Petroleum Science 23 (2026) 2235–2247

Contents lists available at ScienceDirect

Petroleum Science

journal homepage: www.keaipublishing.com/en/journals/petroleum-science

Original Paper

CT investigation on oilwell cement deterioration caused by H_2S along a leaking channel under high temperature: Insights for geothermal applications

Yue Yin [a,b], Li-Wei Zhang [a,b,*], Kai-Yuan Mei [c,d], Xiao-Wei Cheng [c,d], Man-Guang Gan [a,b], Yan Wang [a,b], Chun-Mei Zhang [c,d]

[a] State Key Laboratory of Geomechanics and Geotechnical Engineering Safety, Institute of Rock and Soil Mechanics, Chinese Academy of Sciences, Wuhan, 430071, Hubei, China
[b] University of Chinese Academy of Sciences, Beijing, 100049, China
[c] State Key Laboratory of Oil & Gas Reservoir Geology and Exploitation, Southwest Petroleum University, Chengdu, 610500, Sichuan, China
[d] School of New Energy and Materials, Southwest Petroleum University, Chengdu, 610500, Sichuan, China

ARTICLE INFO

Article history:
Received 21 July 2025
Received in revised form
28 September 2025
Accepted 1 December 2025
Available online 8 December 2025

Edited by Min Li

Keywords:
H_2S
Oilwell cement
High temperature
Computed tomography scanning
Flow-reaction coupling

ABSTRACT

The alteration of oilwell cement due to H_2S poses a significant threat to wellbore structural integrity in geothermal environments. However, laboratory studies on the cement deterioration process caused by H_2S flow along a leaking channel under high-temperature conditions remain scarce. In this study, computed tomography (CT) scanning was utilized to assess the morphological changes and alteration patterns of oilwell cement caused by H_2S flow in multiple dimensions. Additionally, scanning electron microscopy (SEM) coupled with energy-dispersive X-ray spectroscopy (EDS) and Fourier transform infrared spectroscopy (FTIR) were applied to elucidate the microscale mechanisms responsible for the H_2S-driven alteration. The results show that: H_2S flow along the cement channel results in increased cement matrix porosity and formation of large pores, which are especially evident in regions adjacent to the channel. Chemical etching and secondary crystal growth contribute to the expansion of channel dimension and roughening of the channel wall. Consequently, the permeability of the cement matrix exhibited a marked increase of 45% over a period of 14 days. At the microstructural level, compared to unaltered oilwell cement, which exhibits a homogeneous texture and fine particle composition, exposure to H_2S leads to the formation of a heterogeneous and fractured structure within the cement. As a result of sulfidation reactions, a surface layer approximately 1 mm in thickness forms on the cement, which is depleted in calcium and enriched in silicon. The identification of metallic sulfides elucidated the chemical mechanisms responsible for the deterioration of cement properties. In summary, the flow of H_2S through the channel within the cement causes significant alteration of the cement structure compared to other alteration modes.

1. Introduction

Oilwell cement is a critical sealing material used in wellbore construction for geothermal energy extraction, petroleum production, and geological carbon sequestration projects, where maintaining long-term structural integrity is essential (McGrail et al., 2017; Schwartz, 2018; Sigfússon et al., 2018). Oilwell cement provides a hydraulic barrier between the formation and casing, preventing fluid migration and interzonal cross-flow, thereby ensuring safe and efficient fluid management within the wellbore (Ramadan et al., 2019; Su et al., 2023; Eyitayo et al., 2024). A major threat arises from exposure to corrosive gases such as H_2S, which may originate from microbial sulfate reduction, thermochemical processes, thermal degradation, or intentional injection (Yan et al., 2022; Bois et al., 2025). H_2S chemically reacts with cement phases, altering the cement matrix, and can migrate

* Corresponding author.
E-mail address: lwzhang@whrsm.ac.cn (L.-W. Zhang).
Peer review under the responsibility of China University of Petroleum (Beijing).

https://doi.org/10.1016/j.petsci.2025.12.001

through inherent microcracks and other defects in cement, substantially compromising wellbore integrity (Zhang et al., 2013a; Choubineh et al., 2019). H_2S-induced alteration of oilwell cement can result in leakage, environmental contamination, and serious safety hazards, as depicted in Fig. 1.

Due to the highly toxic and corrosive nature of H_2S, research on its effects on the alteration of oilwell cement is limited (Kutchko et al., 2007; Zhang et al., 2013b; Li et al., 2015a). Previous studies on the alteration effects of H_2S on oilwell cement have focused on various aspects, including the evolution of the cement's chemical composition, microstructural changes, degradation of mechanical properties, and the development of preventive measures (Yin et al., 2024). H_2S can penetrate the pores and move along the microcracks in oilwell cement, leading to the dissolution of cement hydration products such as calcium silicate hydrate (C–S–H) and calcium hydroxide (Newell and Carey, 2013). The metal ions from dissolution of hydration products, particularly iron and calcium ions, subsequently react with H_2S to form secondary minerals like pyrite and gypsum (Andreani et al., 2009). Kutchko et al. (2015) proposed that another significant product of the reaction between H_2S and cement is ettringite, which is generated under the effects of "sulfate attack", with sulfate originating from the Fe(III)-induced oxidation of H_2S. These secondary minerals, characterized by poor bonding properties and expansive behaviors, accumulate within the cement matrix, resulting in the formation of microcracks and large pores (Peng et al., 2022). Consequently, this leads to reduced cement strength, increased permeability, and compromised structural stability (Glasser, 1996; Hawthorne et al., 2011; Um et al., 2012). Incorporating additives into cement is a widely adopted strategy for mitigating H_2S-induced cement alteration (Idriss et al., 2001; Liu et al., 2021). The incorporation of additives into cement aims to accomplish three principal goals: reducing permeability, improving chemical stability, and creating physical barriers. Research has demonstrated that materials including nano-silica, nano-clay, asphalt, fibers, and fuzzy-ball fluid loss control additives effectively reduce cement permeability, thus decelerating the alteration process (Lecolier et al., 2010; Mei et al., 2022; Okere et al., 2023). Additives such as silica fume, slag, and fly ash contribute not only to pore filling but also to the reduction of the more susceptible calcium hydroxide, thereby enhancing overall stability (Kutchko et al., 2015). Additionally, the integration of elastic particles like rubber or latex polymers can establish flexible barriers within the cement matrix (Wang et al., 2014). Certain metal compounds undergo alteration in preference to cement hydration products, forming stable compounds and demonstrating a "sacrificial protection" mechanism (Teng et al., 2017; Xu et al., 2018b). Building upon the alteration-inhibiting mechanisms of these materials, ongoing research continues to yield novel protective strategies (Larki et al., 2019; Bois et al., 2025).

The alteration of oilwell cement can be characterized using various technological methods, including CT scanning, SEM, EDS, FTIR, among others (Lecolier et al., 2010; Beck et al., 2016). CT scanning technology is a reliable technique for studying the alteration of porous media (Gan et al., 2020). It allows for the reconstruction of the spatial structure of materials and the calculation of their parameters (Kashim et al., 2019). CT scanning provides an accurate analytical tool for analyzing the alteration processes and microstructural evolution of cement. In the context of interactions between cement-based materials and acidic gases, CT scanning has also been introduced and applied (Um et al., 2012; Andrew et al., 2014; Garing et al., 2017). With high-precision CT scanning systems, the evolution of pore structures during the cement-acid gas reaction can be visually observed (Wang et al., 2013). Applying CT scanning to investigate H_2S-induced alterations along fractures is expected to be efficient. However, it should be noted that CT scanning cannot distinguish minerals with very similar X-ray attenuation values (Gan et al., 2020). Therefore, combining this technique with other methods, such as SEM and FTIR, will facilitate a more precise analysis of the samples (Lebedev et al., 2017). Additionally, most previous studies have focused on static alteration conditions (Kutchko et al., 2011; Um et al., 2012). In the presence of microcracks within the cement, H_2S can induce dynamic alteration of the cement matrix (Andreani et al., 2009).

To date, CT visualization of the alteration process induced by H_2S flow along a leaking channel in oilwell cement, which causes more intense alteration than static conditions and better mimics actual wellbore leaking scenarios, has not been reported. First, the

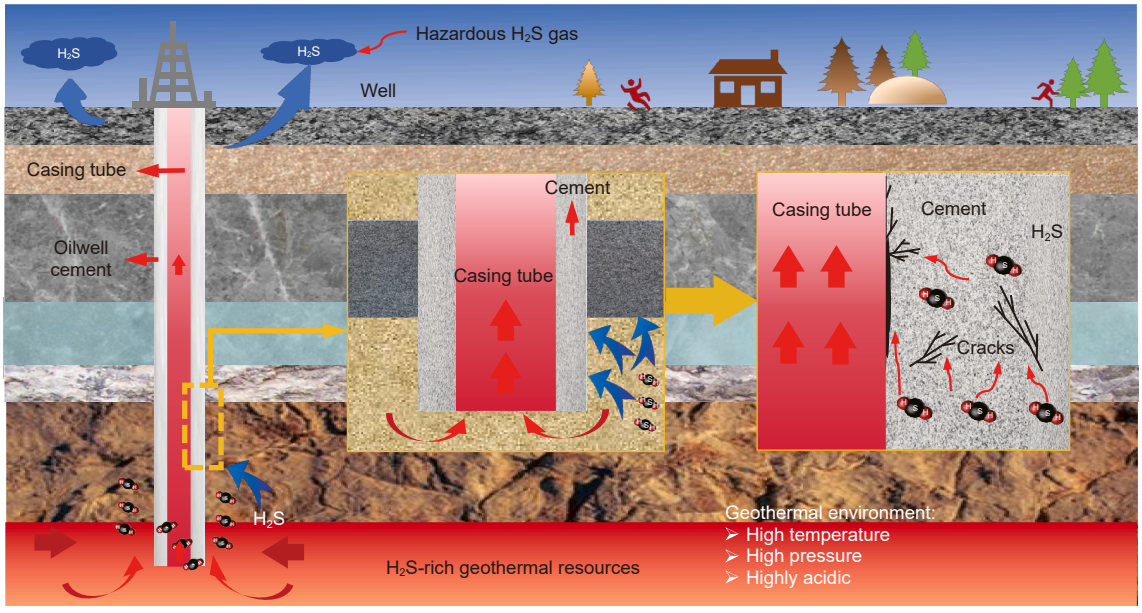

Fig. 1. Leakage in oilwell cement caused by acidic gas alteration.

alteration patterns, morphological features, and underlying chemical and microstructural mechanisms remain poorly understood. Second, the evolution of permeability in the cement matrix due to such flow-driven alteration has not been quantitatively investigated. Furthermore, the effect of high temperature (130 °C or above) on H_2S-induced alteration of oilwell cement has not been adequately investigated in previous studies.

Given these issues, this study aims to investigate the alteration of oilwell cement resulting from H_2S flow along a leaking channel under high-temperature and high-pressure condition. CT scanning was used to assess the alteration patterns and morphological features changes caused by H_2S flow. Subsequently, microstructural evolution induced by H_2S migration was examined using characterization techniques including SEM-EDS and FTIR. Finally, the mechanisms governing H_2S-induced cement alteration under high temperature were elucidated. The findings are expected to provide critical insights for assessing the long-term integrity of wellbore systems in geothermal energy extraction operations.

2. Materials and methods

2.1. Preparation of cement samples

The experiment was conducted using Class G oilwell cement. The composition of the Class G oilwell cement, as determined by X-ray fluorescence (XRF) analysis, is presented in Table 1. A mixture consisting of Class G oilwell cement, quartz sand, silica fume, a dispersant, a water-reducing agent, a defoamer, and water was prepared and thoroughly mixed using a high-speed stirrer. The quartz sand had a fineness of 70 mesh and was added at a dosage of 8% by weight. SiO_2 is the primary component of the quartz sand used in the experiment, with a content exceeding 99%. The silica fume utilized in this study was obtained from a power plant and exhibited an average particle diameter of 0.2 μm and a specific surface area of 24 m^2/g. It was incorporated into the mixture at a concentration of 10% by weight. The chemical composition of the silica fume consisted of more than 96% SiO_2, with impurities comprising metal oxides-including sodium oxide, calcium oxide, iron oxide, and aluminum oxide-as well as trace amounts of elemental carbon and silicon. The total impurity content accounted for less than 4% of the total mass. The incorporation of quartz sand and silica fume into oilwell cement is designed to enhance its overall performance, particularly in terms of high-temperature resistance and alteration durability (Idriss et al., 2001; Liu et al., 2021). The dispersant (G33S) was included at 3% and comprised AMPS, low-molecular weight amides, and polymer-modified polyhydroxy carboxylic acid, while the water-reducing agent (SXY-2) was added at 1.5%, being a powdered ketone-aldehyde polymer that enhances the flowability of the cement slurry. To prevent bubble formation during mixing, the defoamer was introduced at a concentration of 0.05%. The water-to-solid ratio for this experiment was set at 0.44.

The mixed paste was poured into a mold with a diameter of 40 mm and a height of 30 mm, which included a 5 mm diameter flow channel in the middle to simulate H_2S seepage in pre-existing defects within oilwell cement. The prepared cement samples were cured in water at 1 atm and 62 °C for 28 days to promote the hydration process. After curing, the samples were removed and dried for subsequent use.

Table 1
XRF test result of the Class G oilwell cement.

Composition	SiO_2	Al_2O_3	Fe_2O_3	MgO	CaO	K_2O	Na_2O	SO_3
Amount, %	22.31	3.60	4.76	1.29	64.06	0.41	2.48	0.96

2.2. H_2S flow-oilwell cement alteration test

The cured cement samples were placed into the reaction vessel. Photographs of the cured cement sample and the reaction vessel are presented in Fig. 2(a) and (b), respectively. The cement sample was securely fixed against the wall of the vessel using silk threads that wrapped around its exterior, ensuring that the H_2S-containing liquid only flowed through the channel in the middle. The temperature for the H_2S reaction was set at 130 °C, with partial pressures of H_2S and N_2 maintained at 1 and 9 MPa, respectively. This pressure configuration was designed to mimic the conditions of high-sulfur gas reservoirs in China's Sichuan Basin (Huang et al., 2010). Although such reservoirs typically contain significant CO_2 rather than N_2, the present study focuses on elucidating the specific mechanisms of H_2S interaction with oilwell cement. The inclusion of CO_2 was unnecessary and risked obscuring H_2S-specific effects. Therefore, in line with the approaches of Li et al. (2015b), Cheng et al. (2016) and Mei et al. (2019), inert N_2 was used to replace all non-H_2S gases to ensure experimental controllability.

The cement samples were allowed to react with H_2S for a duration of 14 days, during which continuous monitoring was performed to maintain constant gas pressure. Although the duration of the alteration tests was shorter than the actual service life of a wellbore in engineering applications, the results provide valuable reference data for inferring long-term corrosion behavior. First, short-term tests help clarify the mechanisms and characteristics of cement alteration, including the types and morphology of changes, as well as the chemical reactions between cement and H_2S (Li et al., 2015a; Cheng et al., 2016). Furthermore, such tests yield data relevant to long-term changes in actual engineering, which can be used to develop alteration models and supply necessary parameters for numerical simulations. Additionally, short-term tests serve as a comparative benchmark for evaluating different materials or treatment methods, enabling researchers to quickly identify the most effective materials or anti-alteration measures (Xu et al., 2018a; Mei et al., 2019). In previous studies, an alteration duration of 14 days has been commonly adopted, as seen in the work of Mei et al. (2019) and Yin et al. (2024).

2.3. Test methods

2.3.1. CT scanning test

CT scanning was conducted on both the unaltered cement sample (i.e., those not exposed to H_2S) and the cement sample that had been altered by H_2S solution for 14 days. This was done to investigate the structural evolution of oilwell cement under H_2S alteration, particularly focusing on pore distribution, porosity, and the morphology of pore structures. CT scanning is a non-invasive and non-destructive testing technique that utilizes three-dimensional imaging (Miao et al., 2020). It determines the spatial distribution of X-ray attenuation coefficients of an object by measuring its X-ray projections from multiple angles, thereby allowing for the representation of variations in material structure. The analysis of CT images is based on measuring the X-ray attenuation properties of different materials, with results influenced by their atomic numbers and densities (Gan et al., 2024).

In this experiment, a Zeiss Xradia 410X X-ray CT scanner was utilized for CT scanning. The operational parameters of the CT scanner were as follows: 80 kV voltage, 125 μA current, 10 W power, and a voxel size of 11.08 μm. The scanning process involved rotating the samples 360° around the *Z* axis of the workbench in predetermined increments to obtain projection image signals from various angles. Changes in the grayscale values of the CT images were analyzed to identify differences in material density and porosity before and after H_2S alteration. The processing of CT

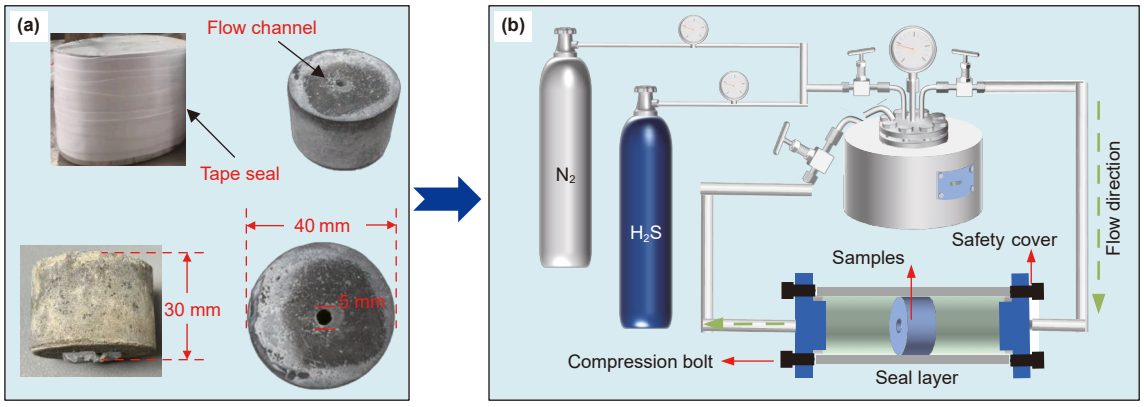

Fig. 2. (a) Dimensions of the cement sample; **(b)** schematic diagram of the oilwell cement alteration testing.

images consisted of data import, denoising filtration, and segmentation, all performed using Avizo software. Segmentation is a vital step in CT data processing, wherein each voxel is categorized into discrete phases corresponding to different material constituents. Histogram-based thresholding, assigning each phase to a specific interval within the grayscale histogram are employed. The segmentation methodology adopted in this study aligns with established approaches reported in prior literature, wherein pores are differentiated from the cement matrix according to variations in grayscale intensity (Wan et al., 2014; Miao et al., 2020; Wang et al., 2021). The segmentation threshold was identified by locating the valley between the first two peaks in the grayscale histogram. The CT scanning system and the method for slicing the samples are illustrated in Fig. 3. Specifically, slices P1 and P4 were taken 1 mm from the top and bottom surfaces of the sample, respectively, while slices P2 and P3 were evenly spaced in the middle of the sample.

2.3.2. Permeability test

Cement samples without artificial channels were selected for permeability testing, so as to understand how H_2S alteration affects the permeability of the oilwell cement. The permeability of the samples was measured using a self-developed pulse permeability testing apparatus. This pulse testing device calculates the permeability coefficient of the sample by establishing the decay curve of the pressure difference across the upstream and downstream of the tested sample over time. The specific method for calculating the permeability coefficient follows the reference (Sun et al., 2018). In this experiment, the effective confining pressure was set at 3.5 MPa, and the pressure difference was set at 0.1 MPa.

2.3.3. SEM-EDS and FTIR tests

CT scanning does have limitations, such as challenges in visualizing materials at the microscopic level and characterizing chemical evolution processes. To address these limitations, CT scanning is supplemented by other advanced techniques such as SEM, EDS, and FTIR to achieve a comprehensive analysis of microstructural evolution of oilwell cement.

Small pieces of oilwell cement samples, both before and after H_2S alteration, were analyzed using SEM and EDS. For SEM analysis, the cement samples were mounted on the observation stage, with observations conducted at magnifications of 100X and 2000X. EDS line scanning was performed from the wall of the flow channel toward the interior of the sample to monitor the weight percentage evolution of elements such as calcium, silicon, and sulfur.

Additionally, some cement samples were finely grounded, and the resultant powders were sieved through a screen with an aperture of 0.075 mm to prepare samples suitable for FTIR phase analysis. The obtained sample powders underwent FTIR testing to analyze and characterize the chemical features of the oilwell cement before and after H_2S alteration.

3. Results

3.1. CT scanning results

3.1.1. Demonstration of CT scanning slices perpendicular to the channel

Fig. 4 illustrates the CT scanning slices of the cement with a leakage channel, captured before and after exposure to H_2S. These images depict the morphology of the cement at various locations before and after H_2S alteration. As the H_2S solution flows through the central channel of the cement, complex cracking patterns emerge near the inlet (as shown in C-P1 in Fig. 4), indicating significant damage to the structural integrity of the cement. The generation of expansive ettringite may lead to the cracking of the cement matrix (Kutchko et al., 2015). The secondary minerals formed through sulfide reactions exhibit weak bonding characteristics with the cement matrix, and under the dynamic flow of the H_2S solution, these minerals may be washed away (Zhang et al., 2014). The changes observed from slices P1 to P4 demonstrate that the alteration effects diminish with increasing distance from the inlet along the flow direction of H_2S. The morphological images indicate that there are no discernible macrocracks in the cement near the outlet (C-P4).

Fig. 5 presents slices illustrating pore distribution extracted from cement sample near the inlet and outlet both before and after the reaction with H_2S. The images have undergone threshold segmentation to enhance the visibility of the pores, which are represented in blue. The porosity of the cement sample prior to exposure to H_2S is significantly lower than that observed after the reaction. Furthermore, the interaction between H_2S and the cement results in a marked increase in the formation of larger pores. This indicates that the reaction not only heightens the internal porosity of the cement but also enlarges the pore sizes. In regions adjacent to the H_2S outlet (Fig. 5(b), C-bottom), small pores can be observed developing near the channel, a phenomenon that is absent in the unaltered sample. In comparison to Figs. 4 and 5 clearly illustrates the accumulation of microcracks near the inlet. These cracks extend from the channel into the cement matrix, displaying variability in their propagation direction; some extend perpendicular to the channel, while others run parallel. Notably,

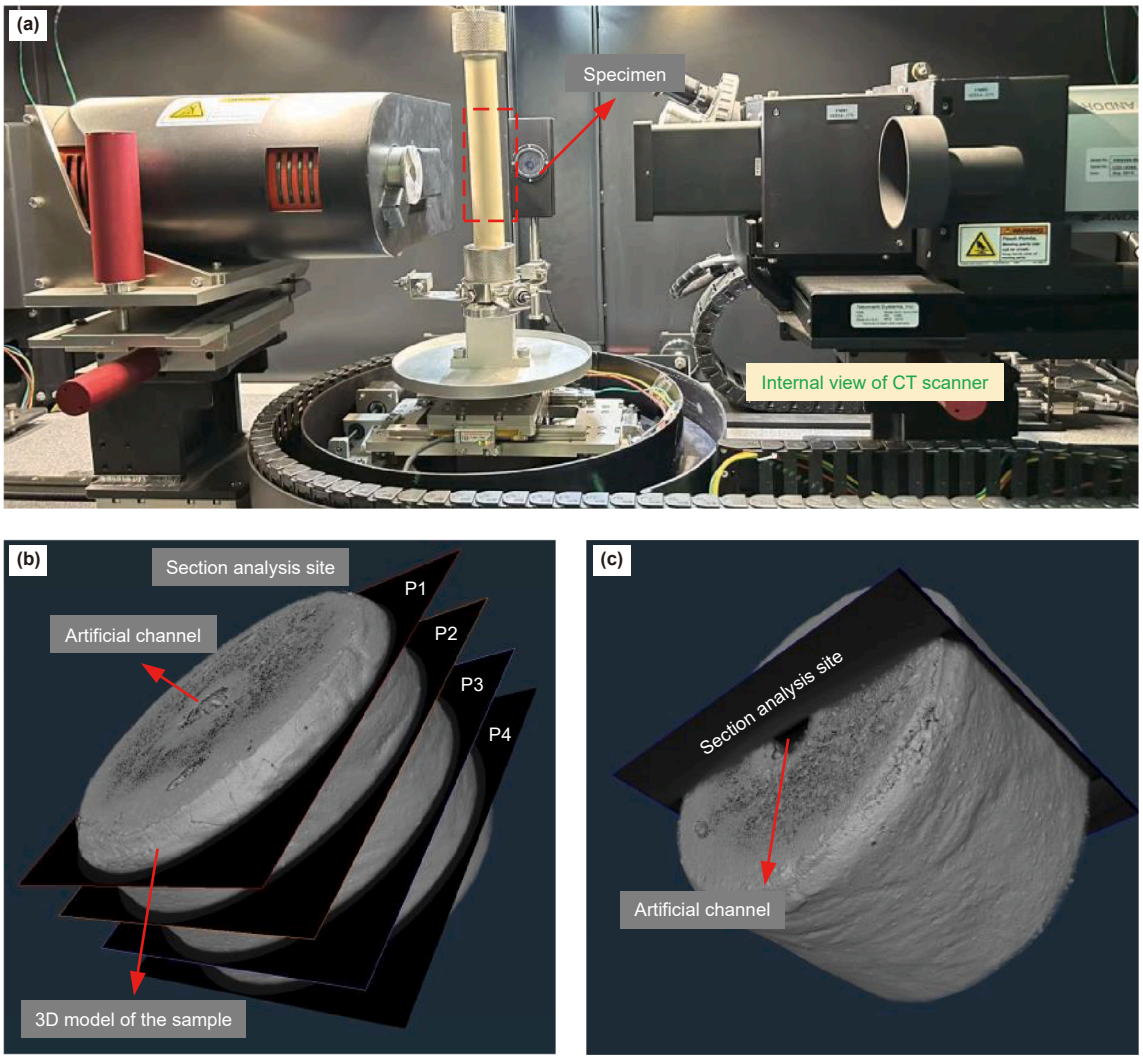

Fig. 3. **(a)** CT scanning testing system, **(b)** sample slices perpendicular to the channel, **(c)** sample slice along the channel.

certain microcracks are continuous, connecting larger pores. The alteration effect of H_2S causes the pore sizes within the cement to expand, thereby creating new weak points. In C-Top of Fig. 5, due to the proximity to the inlet, the effect of H_2S is intensified, resulting in a continual increase in secondary material formation, which exacerbates both dissolution and localized expansion forces. Consequently, this leads to the development of microcracks along the weak points of the pores. The corrosive impact of H_2S on cement mirrors the effects observed with the flow of CO_2 solutions (Gan et al., 2022).

To analyze the distribution of porosity perpendicular to the channel, the area ratio of pores to the total plane area (excluding the channel) was extracted and is presented in Fig. 6. Significant changes in the porosity of the cement sample are observed before and after the reaction with H_2S. Prior to the reaction, the porosity distribution of the cement sample is relatively uniform, with most planes exhibiting porosity in the range of 2%–2.5%. Following the reaction with H_2S, the porosity in the majority of the cement sample has markedly increased, with the maximum porosity observed near the middle of the cement, reaching up to 4.817%. The porosity at the bottom of the sample is the lowest, approaching that of the unaltered sample, while the porosity near the inlet is approximately 3.5%. This value is lower than that in the middle of the cement but higher than at the bottom. This phenomenon can be attributed to the relatively high concentration of corrosive species near the inlet region, which enhances dissolution-precipitation reactions within the cement. Based on conclusions drawn from similar experiments by Yin et al. (2024) this dissolution-precipitation mechanism primarily involves the dissolution of calcium hydroxide and ettringite, along with the precipitation of FeS, FeS_2, and $CaSO_4$. Intensive dissolution and reprecipitation in this zone result in volumetric expansion and microstructural deformation of the cement matrix. The mid-channel region is characterized predominantly by dissolution, leading to gradual consumption of H_2S. As a consequence, the concentration of H_2S decreases toward the bottom of the channel, shifting the dominant reaction mechanism to precipitation and ultimately yielding reduced porosity. It is important to note that the resolution limit of CT scanning is 0.9 mm, and many small pores within the cement have diameters smaller than this threshold, rendering them unidentifiable (Gan et al., 2020). Consequently, the porosity obtained from CT scanning is lower than the actual porosity (Miao et al., 2020). Nonetheless, it remains feasible to utilize the CT scanning results to analyze relative changes in pore characteristics (Wang et al., 2021).

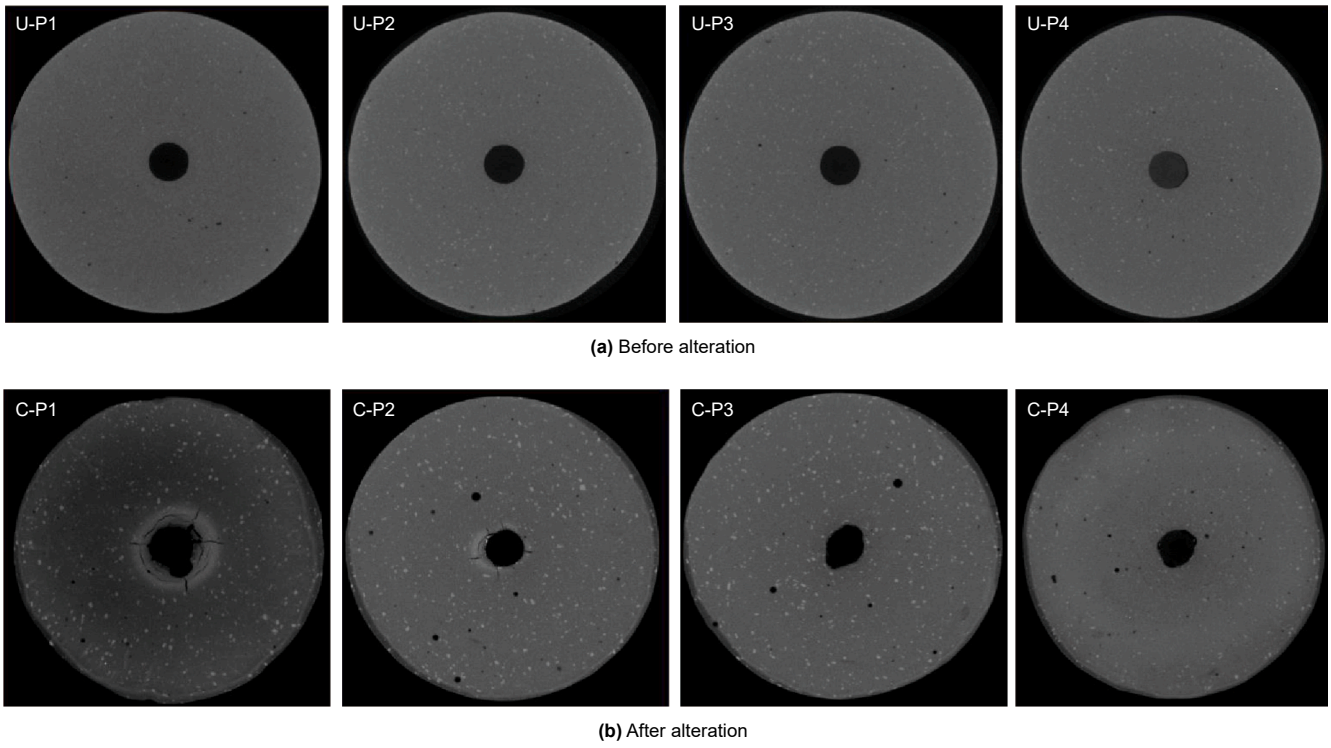

Fig. 4. Slices perpendicular to the channel: **(a)** before alteration; **(b)** after alteration ("C" refers to the sample after reaction with H_2S, and "U" refers to the sample before reaction with H_2S).

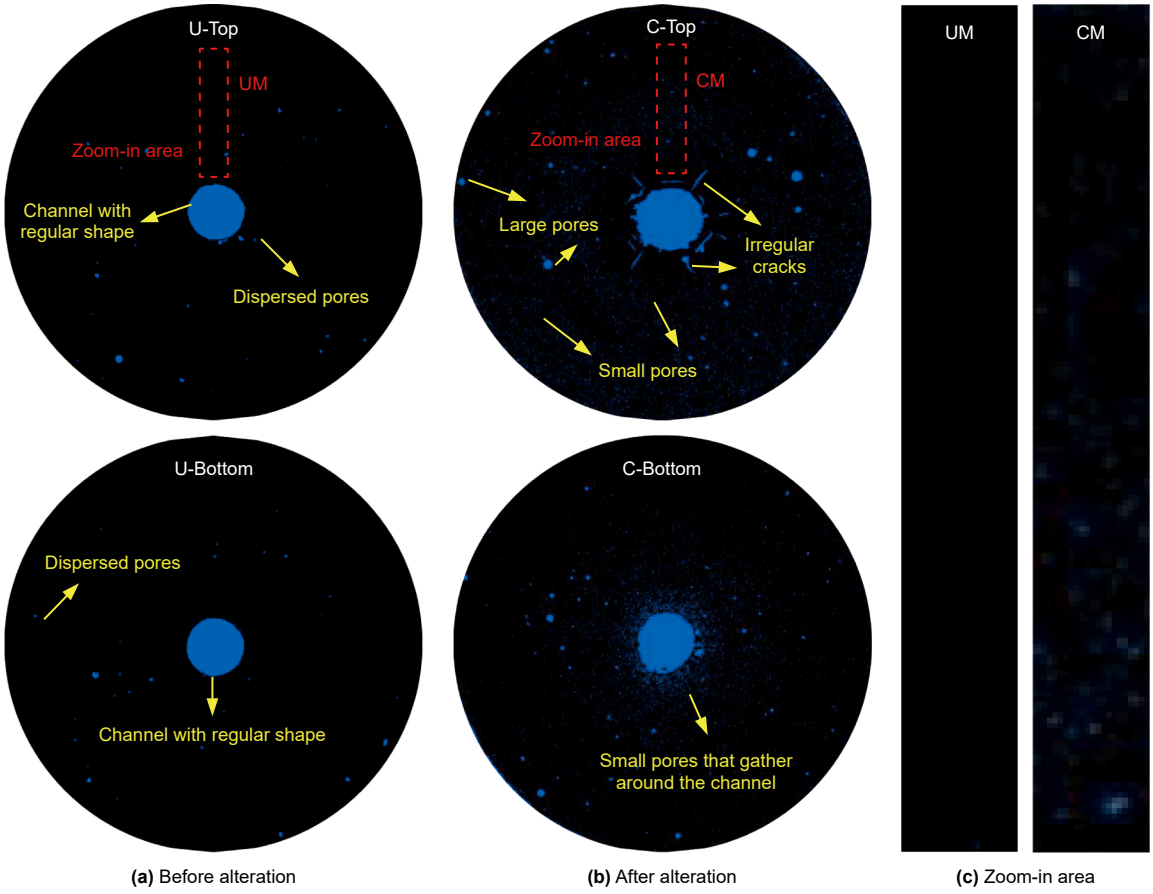

Fig. 5. Pore distribution of slices perpendicular to the channel: **(a)** before alteration; **(b)** after alteration; **(c)** zoom-in area ("C" refers to the sample after reaction with H_2S, and "U" refers to the sample before reaction with H_2S).

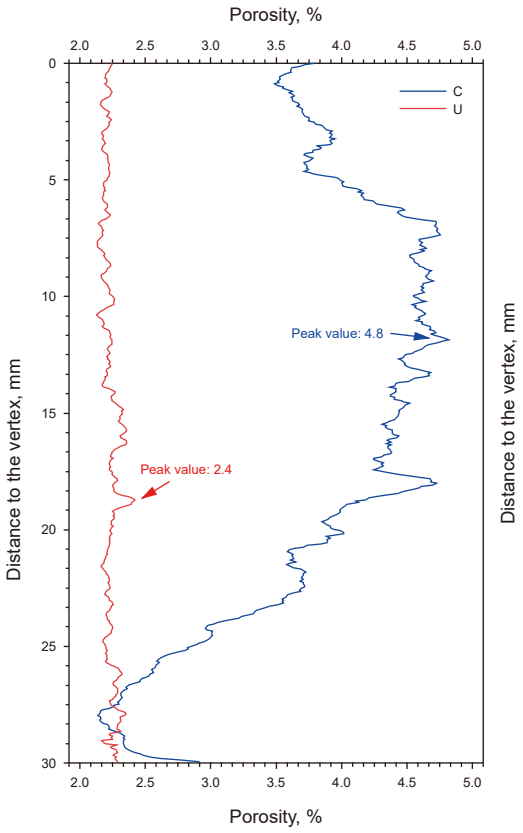

Fig. 6. Pore distribution of slices perpendicular to the channel ("C" refers to the sample after reaction with H_2S, and "U" refers to the sample before reaction with H_2S).

3.1.2. Slices along the channel

H_2S permeates through the channel within the cement, leading to alteration to the cement matrix surrounding the channel. Consequently, it is essential to examine the slices along the channel. Fig. 7 presents morphological images of cement sample slices along the channel before and after exposure to H_2S. After exposure to H_2S, the cement exhibits increased crack propagation and a greater number of larger pores. The cracks situated near the inlet appear to be approximately parallel to the channel within the central region of the cement. The high gray value areas, highlighted in white in the figure, correspond to quartz sand. A comparison of the quartz sand indicates that the gray values of the cement matrix prior to the reaction with H_2S are higher than those observed after the reaction. Some studies suggest that the decrease in gray value of the cement following exposure to acidic media is attributable to an increase in fine pore structures resulting from the reaction (Li et al., 2015b, Miao et al., 2020).

The slices depicted in the previous figure were processed using threshold segmentation to clearly distinguish the pores (depicted in blue) from the matrix (shown in black), as illustrated in Fig. 8. The unaltered cement samples contain fewer pores, which are also smaller in size, and the channel wall surfaces appear relatively smooth. Following alteration by H_2S, there is a notable increase in the overall porosity of the cement sample, characterized by a greater number of larger pores and the emergence of microcracks. The newly formed pores are primarily situated near the channel, while some microcracks extend inward along the channel, with internal microcracks accumulating in regions where pore expansion occurs. The distribution of these cracks in areas adjacent to the alteration indicates that these regions have experienced significant degradation. The alteration of cement by acidic gases leads to varying degrees of modification across different regions (Li et al., 2015b). Furthermore, areas with a high concentration of cracks exhibit a marked increase in the roughness of the cement wall surfaces. It can be reasonably inferred that this change is a consequence of the chemical reactions between H_2S and the chemical composition of the cement, resulting in the dissolution of some primary minerals.

The analysis of Figs. 4–8 indicates that H_2S not only induces significant alteration to the porosity characteristics of the cement matrix but also causes deformation of the channel. Consequently, the entire channel has been segmented, and the ratio of the channel area to the corresponding plane area has been calculated, as illustrated in Fig. 9. In the unaltered cement sample, the flow channel in the central region maintains a generally uniform shape and a smooth surface. However, following exposure to H_2S, the wall roughness of the channel in the middle of the cement increases, resulting in an irregular shape. Near the inlet, the dimensions of the channel expand due to the erosive action of H_2S. In regions adjacent to the inlet, some of the channel areas approximate those of the unaltered sample, which can be attributed to the increase in sample volume after alteration. Significant alteration is also observed in the middle of the channel, leading to an expansion of the channel volume. However, as moves closer to the outlet, this expansion effect gradually decreases. Non-uniform variations in channel volume, attributable to the synergistic effects of chemical etching and secondary crystal growth, have been similarly reported by Gan et al. (2020).

3.2. Permeability of cement matrix

Under the corrosive influence of H_2S, the porosity of oilwell cement increases, subsequently leading to enhanced permeability of the cement matrix. Cylindrical cores were extracted from

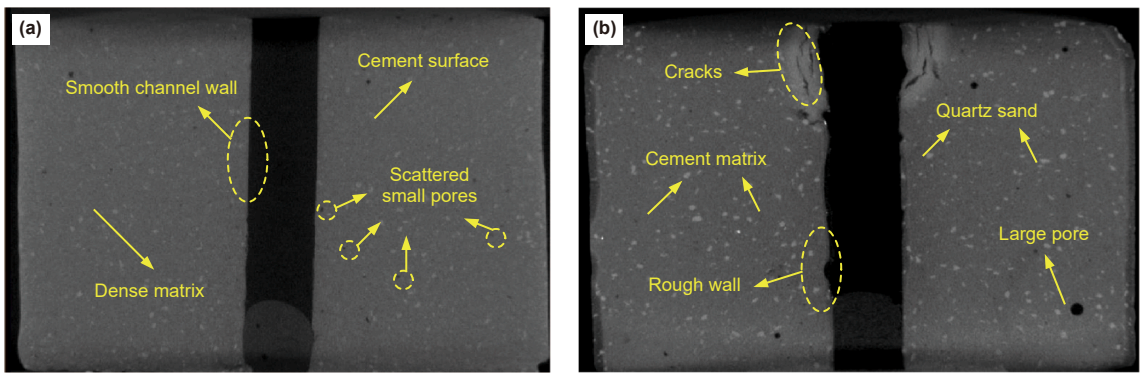

Fig. 7. Slices along the channel: **(a)** before alteration; **(b)** after alteration.

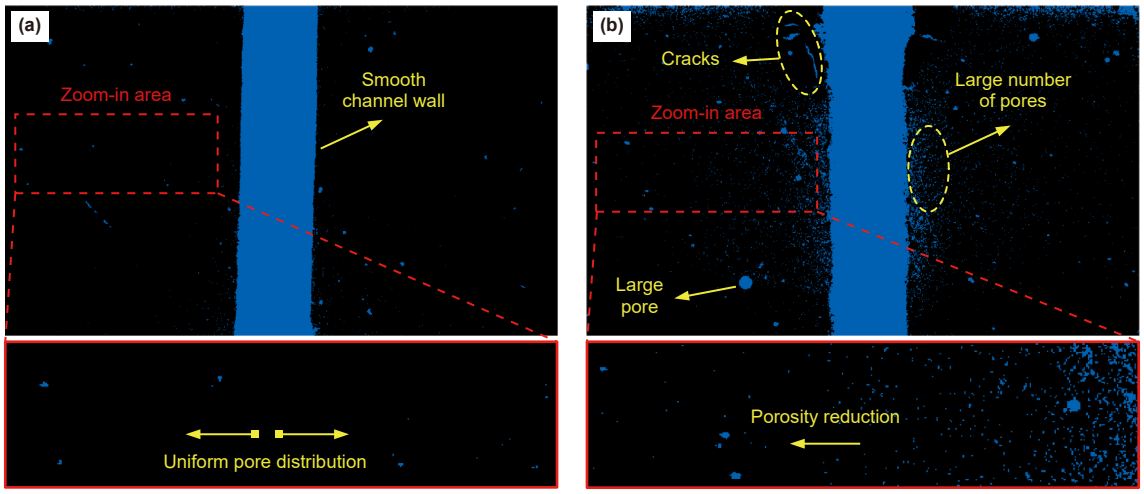

Fig. 8. Pore distribution of slices along the channel: **(a)** before alteration; **(b)** after alteration.

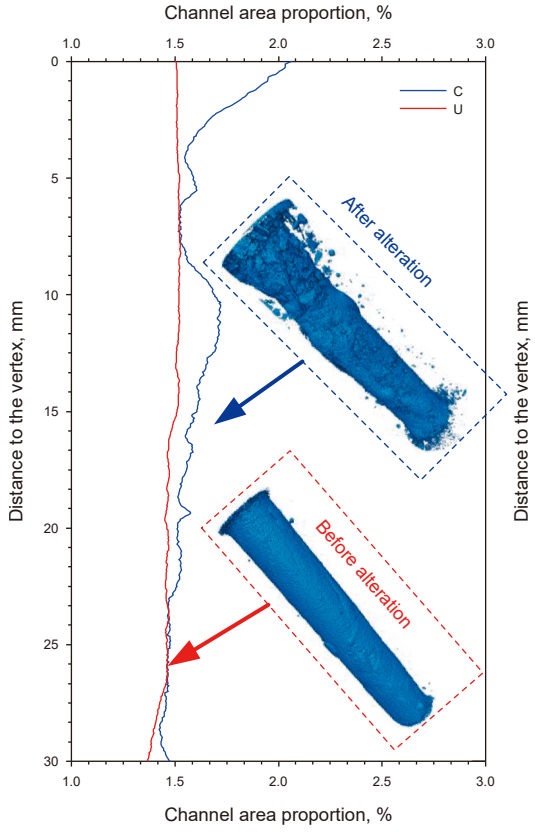

Fig. 9. Changes in channel dimensions and comparison of 3D structures ("C" refers to the sample after reaction with H_2S, and "U" refers to the sample before reaction with H_2S).

cement sample that had undergone alteration by H_2S. These samples, along with unaltered cement samples of equivalent dimensions, were subjected to permeability testing. Notably, the samples used for permeability testing did not contain any channel; therefore, the reported permeability values reflect the permeability of the cement matrix. For each category, three samples were tested, one set consisting of cement samples altered by H_2S for 14 days, and another set comprising unaltered cement samples. This approach was adopted to yield average permeability values and minimize error. The results of the permeability tests are presented in Table 2. The permeability values of the unaltered cement samples were recorded as 0.064, 0.059, and 0.056 mD, yielding an average value of 0.060 mD. In contrast, the permeability values of the cement samples altered by H_2S for 14 days were 0.091, 0.086, and 0.083 mD, resulting in an average value of 0.087 mD. Compared to the unaltered samples, the average permeability of the cement samples altered by H_2S for 14 days increased by 45%. Unlike CO_2, which may cause pore blockage and subsequently reduce the permeability of cement, H_2S markedly enhances the permeability of cement (Xu et al., 2018a).

Table 2
Permeability of cement matrix.

Sample name	Permeability, mD	
	Value	Average value
U-#1	0.064	0.060
U-#2	0.059	
U-#3	0.056	
C-#1	0.091	0.087
C-#2	0.086	
C-#3	0.083	

3.3. Microstructure and chemical test results

3.3.1. SEM test results

CT scanning results illustrate the overall structural changes in the cement; however, they fall short in displaying the morphological changes at specific locations within the material. To address this limitation, SEM experiments were conducted to examine the microstructural differences in the cement caused by H_2S exposure. Fig. 10 presents SEM images of the cement samples before and after the reaction with H_2S. As shown in Fig. 10(a), the unaltered cement exhibits a uniform texture characterized by low porosity and a minimal number of large pores. When magnified 2000 times, as depicted in Fig. 10(b), the cement particles appear fine, exhibiting few pores with no significant voids present. The structural integrity of the cement sample is well preserved, with virtually no microcracks observed. Conversely, the cement following the reaction with H_2S, as illustrated in Fig. 10(c), reveals the formation of larger pores. A comparison between the edges and the interior of the sample indicates that the porosity and the abundance of large pores at the edges are significantly lower than those found in the interior. When

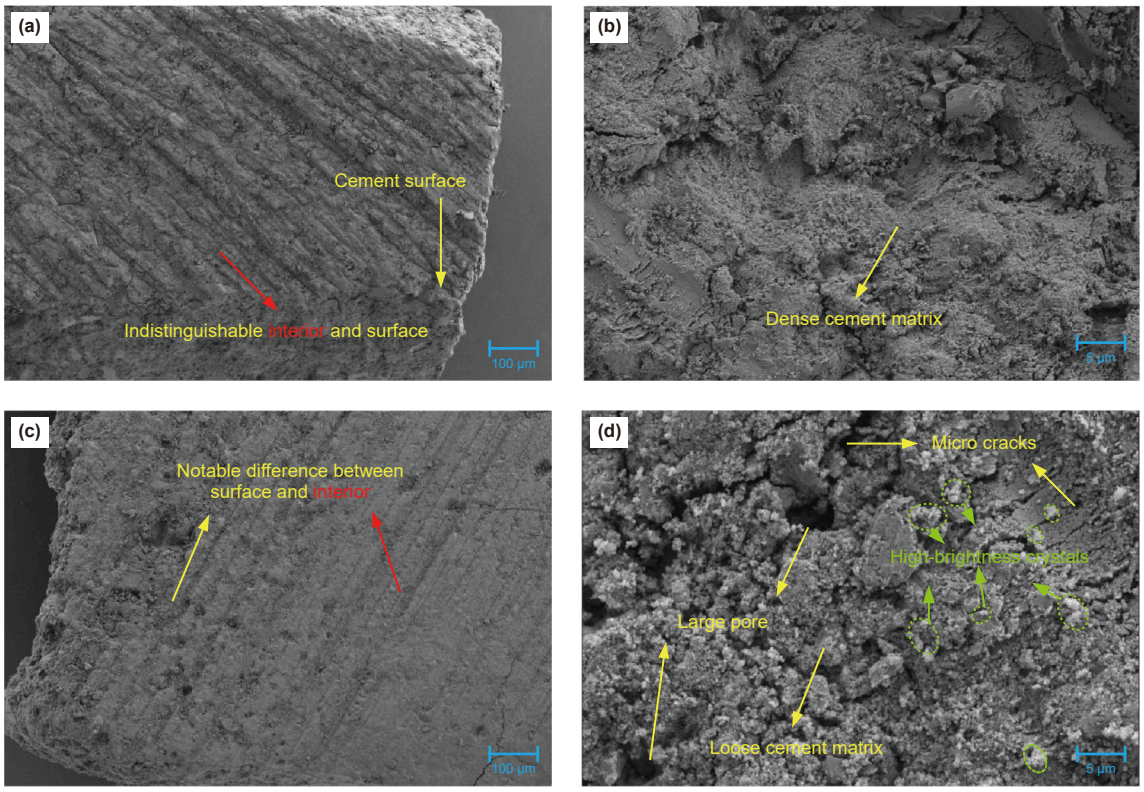

Fig. 10. SEM images of the oilwell cement: **(a)** before alteration, magnification 100X; **(b)** before alteration, magnification 2000X; **(c)** after alteration, magnification 100X; **(d)** after alteration, magnification 2000X.

localized areas are examined at the same magnification (2000 times), as seen in Fig. 10(d), the microstructure of the cement post-alteration appears markedly different from that prior to alteration. The altered cement exhibits larger pores, cracks, and a transformation of the cement material into unevenly fragmented larger particles. This microstructural transformation is typical of cement altered by acid gases (Li et al., 2015b). Additionally, the conspicuous formation of new, high-brightness crystals, likely identified as FeS and FeS_2 based on the study by Yin et al. (2024) indicates that the reaction between H_2S and cement follows a dissolution-precipitation mechanism rather than adsorption. This further suggests that sulfur is incorporated into the crystal lattice rather than being surface-adsorbed. The structural integrity of the cement is significantly compromised after the reaction with H_2S. These findings underscore the pronounced impact of H_2S on the physical and chemical stability of the cement. The mineral alterations that occur in the aftermath of H_2S exposure not only modify the cement's microstructure but also adversely affect its sealing capacity and durability under prolonged service conditions.

3.3.2. EDS test results

EDS element scanning provides a visual representation of the elemental distribution changes within the cement. As depicted in Fig. 11(a), the Ca/Si ratio in unaltered cement is relatively similar. When the EDS scanning is conducted from the channel wall surface towards the internal, the Ca/Si ratio ranges approximately from 1 to 3. In contrast, following exposure to H_2S, the Ca/Si ratio in the cement decreases, as shown in Fig. 11(b). EDS line scanning from the interior to the channel wall surface reveals a gradual decline in this ratio. This reduction indicates that calcium ions are leaching from the cement matrix. Previous studies have established that the interaction between H_2S and cement facilitates the precipitation of metal ions (Zhang et al., 2013a; Kutchko et al., 2015). These metal ions can react with sulfide ions or sulfate ions produced from the dissolution of H_2S, resulting in the formation of new substances (Yin et al., 2024). Notably, the estimated thickness of the decalcification zone on the cement surface is approximately 1 mm. The phenomenon of acid gases leading to delamination in cement structures has been noted, and additional findings reinforce this observation (Kutchko et al., 2007). However, this does not suggest that the alteration depth of H_2S is confined to 1 mm, as the EDS scan results for sulfur demonstrate that the stable distribution of S element extends further into the cement, as illustrated in Fig. 11(c). The increase in porosity further supports the depth of H_2S-induced alteration. This phenomenon can be explained by the reaction of H_2S with the cement upon contact, leading to the leaching of metallic ions that are continuously carried away, forming a decalcified layer near the channel wall. Subsequently, H_2S penetrates the interior of the cement sample, causing the internal metallic ions to migrate toward the channel and resulting in the dissolution of the cement's native substances, ultimately increasing porosity.

3.3.3. FTIR test results

FTIR is highly sensitive to chemical bonds and can effectively analyze the material changes in cement samples before and after alteration by H_2S. Fig. 12 presents a comparison of the FTIR results for unaltered cement samples with those altered by H_2S for 14 days. Characteristic peaks are present in both samples at 3396, 1636, 1421, 961, 873, and 619 cm^{-1}. The peak at 3396 cm^{-1} is typically associated with the stretching vibration of O–H groups, indicative of calcium hydroxide's presence in the cement. The peak at 1636 cm^{-1} likely pertains to the bending vibration of O–H in bound water. The peak at 1421 cm^{-1} primarily corresponds to the

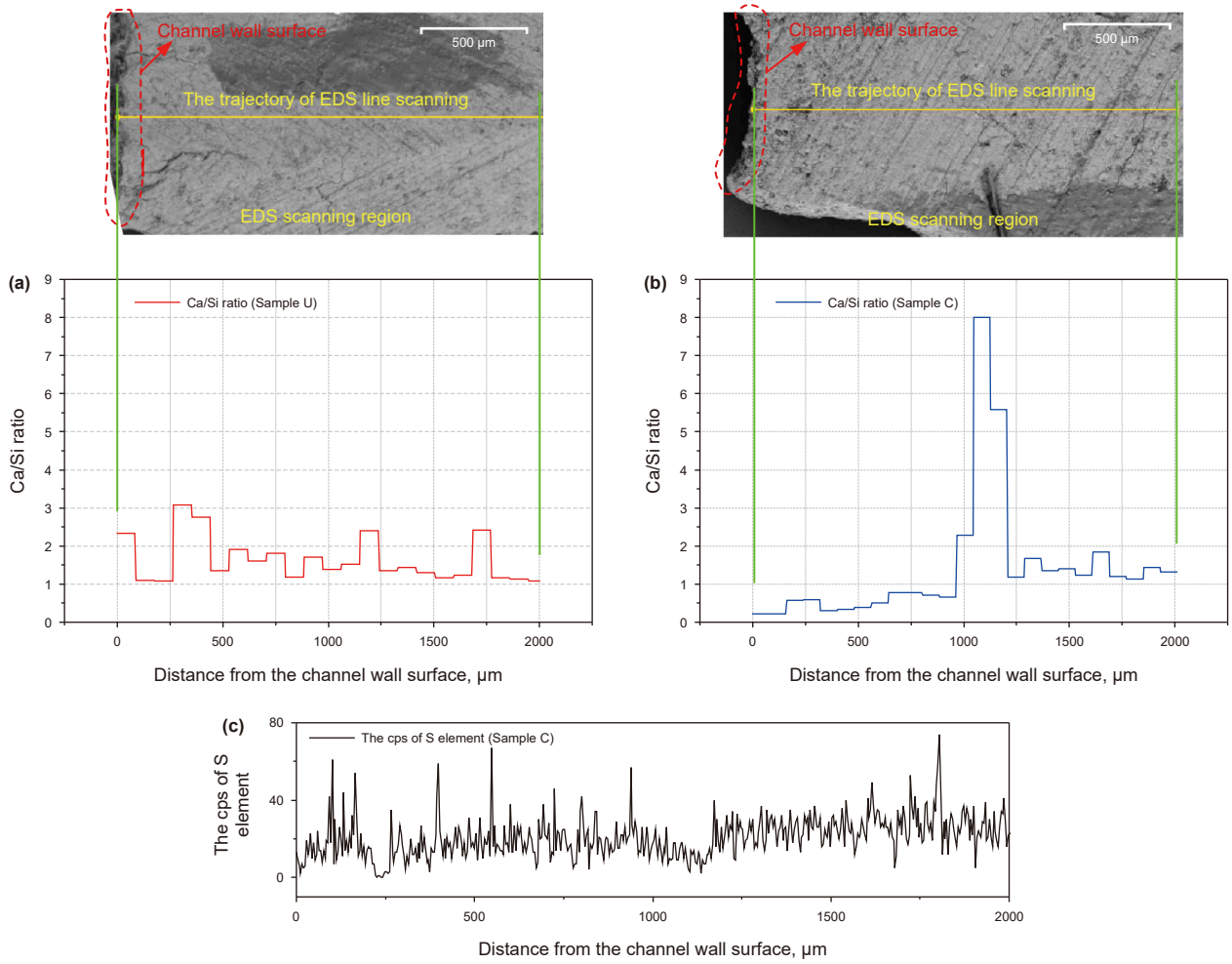

Fig. 11. EDS line scanning results of the oilwell cement: **(a)** Ca/Si ratio before alteration; **(b)** Ca/Si ratio after alteration; **(c)** the cps (counts per second) of sulfur (S) element (cps is used to quantify the concentration of elements within a sample) ("C" refers to the sample after reaction with H_2S, and "U" refers to the sample before reaction with H_2S).

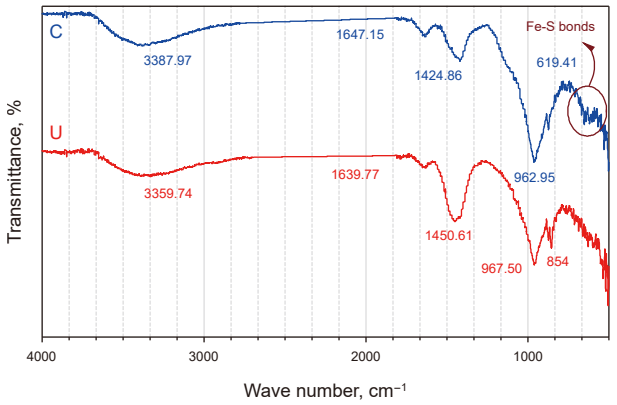

Fig. 12. FTIR test results ("C" refers to the sample after reaction with H_2S, and "U" refers to the sample before reaction with H_2S).

stretching vibration of C–O. The peaks at 961 and 873 cm^{-1} are characteristic absorption peaks typically linked to Si–O or S–O bonds, which may arise from sulfur-cement derivatives or sulfate compounds. The peak at 619 cm^{-1}, positioned within the low-frequency range, is associated with the vibrational modes of Fe–S bonds. This observation aligns with findings from previous studies indicating the formation of metal sulfides as a result of the interaction between H_2S and cement (Jacquemet et al., 2012). Generally, oilwell cement does not produce sulfides following hydration (Taylor, 1965; Guner et al., 2017). However, sulfides generated from the alteration of cement by H_2S, can significantly impact the mechanical properties and microstructure of the cement samples, leading to increased porosity and decreased strength (Jung and Um, 2013). Experiments conducted by Yin et al. (2024) under comparable conditions demonstrated that H_2S induces the dissolution of calcium hydroxide and ettringite in oilwell cement, along with the formation of FeS, FeS_2, and $CaSO_4$. Notably, the formation of thaumasite, a sulfate attack product typically observed in cement under low-temperature conditions, was not detected, as this phase is thermodynamically unstable at high temperatures.

4. Discussion

During the seepage alteration of H_2S along the cement channel, the porosity on both sides of the channel is observed to increase, with a proliferation of larger pores. The alteration effects are more pronounced as proximity to the channel increases. Following H_2S alteration, the channel walls exhibit roughening, and the sizes of the channel expand. The microstructural changes in cement, as evidenced by FTIR in this study and supported by earlier results from Yin et al. (2024) on H_2S-cement interactions under flowing

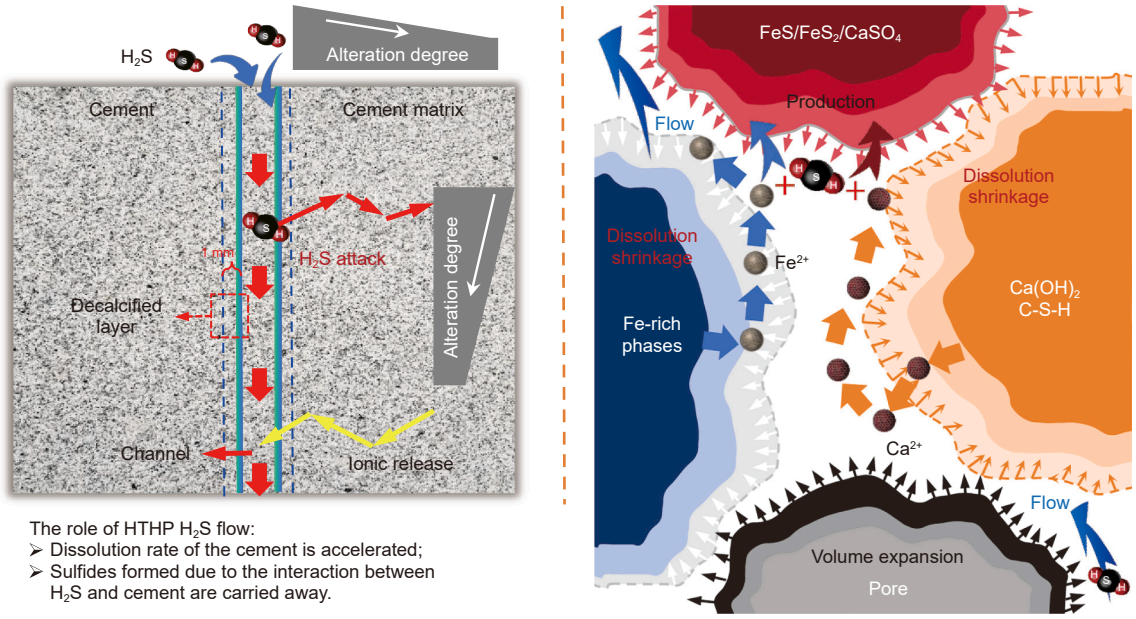

Fig. 13. Schematic representation of cement alteration induced by the flow of H_2S along the channel.

conditions, are consistent with a chemical mechanism involving dissolution of ettringite and $Ca(OH)_2$, coupled with precipitation of FeS, FeS_2, and $CaSO_4$. The incorporation of sulfur into the crystal lattice renders the deleterious effects of this chemical process persistent.

The flow alteration of cement by H_2S in this study has a pronounced effect, which supplements previous results from one-phase alteration tests (Li et al., 2015a), immersion alteration tests (Zhang et al., 2013b), and dry gas alteration tests (Hawthorne et al., 2011). By comparing the dynamic alteration results of this study with prior static alteration findings, it was determined that flow-induced alteration by H_2S results in more pronounced degradation of the cement (Ji and Zhu, 2013; Xu et al., 2018a). This phenomenon has also been observed in certain studies concerning the flow-induced alteration of CO_2 along channel within cement (Gan et al., 2022). This increased degradation may be attributed to the flowing acidic gas solution, which transports away ions leached from the cement, thus perpetuating the dissolution process of the cement. Conversely, in static reactions, a decrease in the reaction rate between acidic gases and cement has been noted, potentially due to the blockage of certain pores by secondary biomass (Jacquemet et al., 2012; Zhang et al., 2013a). The surfaces of the cement that come into direct contact with the H_2S solution may become entirely decalcified, while the hydration products within the cement continue to dissolve, migrate toward the channels, and are ultimately removed. This leads to an increase in both the porosity and permeability of the cement matrix, accompanied by the development of structural layering. The flow-alteration process is illustrated and summarized in Fig. 13. As is known from previous studies, $Ca(OH)_2$ reacts rapidly with H_2S and contributes most significantly to the early-stage evolution of the pore structure (Zhang et al., 2013b; Kutchko et al., 2015). In contrast, the degradation of C–S–H gel results in prolonged and fundamental weakening of the cement matrix, accompanied by continuous development of the pore network (Jacquemet et al., 2012). Furthermore, the dissolution of the cement results in a decline in the alteration resistance of the substrate (Yin et al., 2024). Therefore, the flow-induced alteration of cement by H_2S warrants significant attention.

Previous studies on the alteration of oilwell cement by H_2S have primarily focused on lower temperatures, such as 50, 90, and 100 °C, among others (Kutchko et al., 2011, 2015; Zhang et al., 2014). In the context of geothermal resource extraction, a temperature of 130 °C is classified as moderate-temperature geothermal. In environments with abundant H_2S, the synergistic effects of high temperature, high pressure, and flow continuously facilitate the alteration of the cement (Zhang et al., 2023). This finding holds significant implications for high-temperature geothermal extraction, oil and gas field development.

5. Conclusions

An experiment was conducted to investigate the alteration of oilwell cement induced by the flow of H_2S through an artificial channel within cement in a high-temperature, high-pressure reactor. Advanced characterization techniques, including CT scanning, SEM, EDS, and FTIR, were employed to analyze the effects of H_2S alteration on the microstructure, permeability, and chemical composition of the oilwell cement. The main conclusions are as follows.

(1) The flow of H_2S through the artificial channel in the oilwell cement leads to an increase in porosity and an expansion of pore sizes within the cement matrix surrounding the channel. This alteration is particularly pronounced near the channel wall. H_2S induces chemical etching and secondary crystal growth within the cement matrix, causing an enlargement of channel dimensions and increased surface roughness along the channel wall. The effects of H_2S result in significant swelling and cracking of the cement near the flow inlet, thereby compromising the structural integrity of the cement material.

(2) The alteration effect of H_2S significantly increases the permeability of the cement matrix. The average permeability of the cement prior to alteration, under an effective confining pressure of 3.5 MPa, is measured at 0.060 mD. In contrast, the average permeability of cement samples altered by H_2S for 14 days is recorded at 0.087 mD,

indicating a 45% increase in permeability as a result of H_2S alteration. This phenomenon can be attributed to H_2S causing the internal pores of the oilwell cement to expand, thereby increasing porosity and facilitating the initiation of micro-cracks.

(3) Unaltered oilwell cement displays a uniform texture, characterized by fine particles, low porosity, and a scarcity of large pores at the microscopic level. In contrast, exposure to H_2S results in the formation of larger pores and cracks within the cement, causing the cement material to exhibit an uneven and fragmented appearance. Additionally, a decalcified, silica-rich layer approximately 1 mm thick forms on the surface of the channel wall as a result of the sulfidation reaction. The detection of metal sulfides in FTIR analyses elucidates the chemical mechanisms underlying the deterioration of the cement's properties.

The findings of this study can be extrapolated to more complex wellbore engineering scenarios, providing important insights for evaluating the corrosion patterns and mechanisms associated with high-temperature H_2S flow along leaking channels. However, further development of this experiment is necessary. Future analyses should focus on the mechanisms through which H_2S contributes to the reduction in the strength of oilwell cement. Additionally, subsequent studies should aim to provide insights regarding the influences of temperature and pressure, especially for the conditions of extreme high temperature and high pressure.

CRediT authorship contribution statement

Yue Yin: Writing – original draft, Methodology, Investigation, Conceptualization. **Li-Wei Zhang:** Writing – review & editing, Supervision, Resources, Methodology, Conceptualization. **Kai-Yuan Mei:** Methodology, Investigation. **Xiao-Wei Cheng:** Supervision. **Man-Guang Gan:** Software. **Yan Wang:** Resources. **Chun-Mei Zhang:** Resources.

Declaration of interests

The authors declare that they have no known competing financial interests or personal relationships that could have appeared to influence the work reported in this paper.

Acknowledgements

The authors are grateful for the funding support provided by National Natural Science Foundation of China (Project No. 42172315), CNPC Innovation Fund (Project No. 2024DQ02-0141) and Chinese Academy of Sciences International Collaboration Project (Project No. 026GJHZ2024018MI).

References

Andreani, M., Luquot, L., Gouze, P., et al., 2009. Experimental study of carbon sequestration reactions controlled by the percolation of CO_2-rich brine through peridotites. Environ. Sci. Technol. 43, 1226–1231. https://doi.org/10.1021/es8018429.

Andrew, M., Bijeljic, B., Blunt, M.J., 2014. Pore-scale contact angle measurements at reservoir conditions using X-ray microtomography. Adv. Water Resour. 68, 24–31. https://doi.org/10.1016/j.advwatres.2014.02.014.

Beck, J., Feng, R., Hall, D.M., et al., 2016. Effects of H_2S and CO_2 on cement/casing interface corrosion integrity for cold climate oil and gas well applications. ECS Trans. 72, 107–122. https://doi.org/10.1149/ma2016-01/15/946.

Bois, A.P., James, S., Badalamenti, A., 2025. Chapter 6 - High-temperature geothermal well cementing. In: Livescu, S., Dindoruk, B. (Eds.), Geothermal Energy Engineering. Elsevier, Leiden, pp. 129–179. https://doi.org/10.1016/B978-0-443-21662-6.00005-0.

Cheng, X., Mei, K., Li, Z., et al., 2016. Research on the interface structure during unidirectional corrosion for oil-well cement in H_2S based on computed tomography technology. Ind. Eng. Chem. Res. 55, 10889–10895. https://doi.org/10.1021/acs.iecr.6b02162.

Choubineh, A., Helalizadeh, A., Wood, D.A., 2019. Estimation of minimum miscibility pressure of varied gas compositions and reservoir crude oil over a wide range of conditions using an artificial neural network model. Adv. Geo-Energy Res. 3, 52–66. https://doi.org/10.26804/ager.2019.01.04.

Eyitayo, S.I., Talal, G., Kolawole, O., et al., 2024. Experimental investigation of the impact of CO_2 injection strategies on rock wettability alteration for CCS applications. Energies 17. https://doi.org/10.3390/en17112600.

Gan, M., Zhang, L., Miao, X., et al., 2020. Application of computed tomography (CT) in geologic CO_2 utilization and storage research: a critical review. J. Nat. Gas Sci. Eng. 83, 103591. https://doi.org/10.1016/j.jngse.2020.103591.

Gan, M., Zhang, L., Wang, Y., et al., 2022. 3D micro-structural changes of an artificial flow channel in wellbore cement under geologic CO_2 storage conditions: combined effect of effective stress and flow. Constr. Build. Mater. 325, 126761. https://doi.org/10.1016/j.conbuildmat.2022.126761.

Gan, M., Zhang, L., Wang, Y., et al., 2024. Experimental study on the corrosion behavior of wellbore cement with a leaking channel under different acidic environments. Int. J. Greenh. Gas Control 139, 104267. https://doi.org/10.1016/j.ijggc.2024.104267.

Garing, C., Voltolini, M., Ajofranklin, J.B., et al., 2017. Pore-scale evolution of trapped CO_2 at early stages following imbibition using micro-CT imaging. Energy Proc. 114, 4872–4878. https://doi.org/10.1016/j.egypro.2017.03.1628.

Glasser, F.P., 1996. The role of sulfate mineralogy and cure temperature in delayed ettringite formation. Cem. Concr. Compos. 18, 187–193. https://doi.org/10.1016/0958-9465(96)00015-7.

Guner, D., Ozturk, H., Erkayaoglu, M., 2017. Investigation of the elastic material properties of class G cement. Struct. Concr. 18. https://doi.org/10.1002/suco.201600020.

Hawthorne, S.B., Miller, D.J., Holubnyak, Y., et al., 2011. Experimental investigations of the effects of acid gas (H_2S/CO_2) exposure under geological sequestration conditions. Energy Proc. 4, 5259–5266. https://doi.org/10.1016/j.egypro.2011.02.505.

Huang, S., Liao, F., Wu, X., et al., 2010. Distribution characteristics of hydrogen sulphide-bearing gas pools and the genesis of hydrogen sulphide in Sichuan Basin. Nat. Gas Geosci. 21, 705–714. https://doi.org/10.11764/j.issn.1672-1926.2010.05.705 (in Chinese).

Idriss, A.F., Negi, S.C., Jofriet, J.C., et al., 2001. SE-structures and environment: corrosion of steel reinforcement in mortar exposed to hydrogen sulphide, part 2: diffusion tests. J. Agric. Eng. Res. 79, 341–348. https://doi.org/10.1006/jaer.2001.0712.

Jacquemet, N., Pironon, J., Lagneau, V., et al., 2012. Armouring of well cement in H_2S-CO_2 saturated brine by calcite coating-experiments and numerical modelling. Appl. Geochem. 27, 782–795. https://doi.org/10.1016/j.apgeochem.2011.12.004.

Ji, X., Zhu, C., 2013. Predicting possible effects of H_2S impurity on CO_2 transportation and geological storage. Environ. Sci. Technol. 47, 55–62. https://doi.org/10.1021/es301292n.

Jung, H.B., Um, W., 2013. Experimental study of potential wellbore cement carbonation by various phases of carbon dioxide during geologic carbon sequestration. Appl. Geochem. 35, 161–172. https://doi.org/10.1016/j.apgeochem.2013.04.007.

Kashim, M.Z., Giwelli, A., Clennell, B., et al., 2019. Determining critical flowrate in high CO_2 content carbonate field, Sarawak basin, offshore East Malaysia. In: Int. Pet. Technol. Conf. 2019. IPTC. https://doi.org/10.2523/iptc-19422-ms, 2019.

Kutchko, B.G., Strazisar, B.R., Dzombak, D.A., et al., 2007. Degradation of well cement by CO_2 under geologic sequestration conditions. Environ. Sci. Technol. 41, 4787–4792. https://doi.org/10.1021/es062828c.

Kutchko, B.G., Strazisar, B.R., Hawthorne, S.B., et al., 2011. H_2S-CO_2 reaction with hydrated class H well cement: acid-gas injection and CO_2 Co-sequestration. Int. J. Greenh. Gas Control 5, 880–888. https://doi.org/10.1016/j.ijggc.2011.02.008.

Kutchko, B.G., Lopano, C.L., Strazisar, B.R., et al., 2015. Impact of oil well cement exposed to H_2S saturated fluid and gas at high temperatures and pressures: implications for acid gas injection and Co-sequestration. J. Sustain. Energy Eng. 3, 80–101. https://doi.org/10.7569/jsee.2015.629509.

Larki, O., Apourvari, S.N., Schaffie, M., et al., 2019. A new formulation for lightweight oil well cement slurry using a natural pozzolan. Adv. Geo-Energy Res. 3, 242–249. https://doi.org/10.26804/ager.2019.03.02.

Lebedev, M., Zhang, Y., Sarmadivaleh, M., et al., 2017. Carbon geosequestration in limestone: pore-scale dissolution and geomechanical weakening. Int. J. Greenh. Gas Control 66, 106–119. https://doi.org/10.1016/j.ijggc.2017.09.016.

Lecolier, E., Rivereau, A., Ferrer, N., et al., 2010. Durability of oilwell cement formulations aged in H_2S-containing fluids. SPE Drill. Complet. 25 (1), 90–95. https://doi.org/10.2118/99105-PA.

Li, Q., Lim, Y.M., Jun, Y.S., 2015a. Effects of sulfate during CO_2 attack on Portland cement and their impacts on mechanical properties under geologic CO_2 sequestration conditions. Environ. Sci. Technol. 49, 7032–7041. https://doi.org/10.1021/es506349u.

Li, Z., Gu, T., Guo, X., et al., 2015b. Characterization of the unidirectional corrosion of oilwell cement exposed to H_2S under high-sulfur gas reservoir conditions. RSC Adv. 5, 71529–71536. https://doi.org/10.1039/c5ra12481f.

Liu, H., Bu, Y., Zhou, A., et al., 2021. Silica sand enhanced cement mortar for cementing steam injection well up to 380 °C. Constr. Build. Mater. 308, 125142. https://doi.org/10.1016/j.conbuildmat.2021.125142.

McGrail, B.P., Schaef, H.T., Spane, F.A., et al., 2017. Field validation of supercritical CO_2 reactivity with basalts. Environ. Sci. Technol. Lett. 4, 6–10. https://doi.org/10.1021/acs.estlett.6b00387.

Mei, K., Cheng, X., Zhang, L., et al., 2019. Self-healing mechanism of Zn-enhanced cement stone: an application for sour natural gas field. Constr. Build. Mater. 227, 116651. https://doi.org/10.1016/j.conbuildmat.2019.08.032.

Mei, K., Zhang, L., Wang, Y., et al., 2022. Structural evolution in micro-calcite bearing Ca-montmorillonite reinforced oilwell cement during CO_2 invasion. Constr. Build. Mater. 315, 125744. https://doi.org/10.1016/j.conbuildmat.2021.125744.

Miao, X., Zhang, L., Wang, Y., et al., 2020. Characterisation of wellbore cement microstructure alteration under geologic carbon storage using X-ray computed micro-tomography: a framework for fast CT image registration and carbonate shell morphology quantification. Cem. Concr. Compos. 108, 103524. https://doi.org/10.1016/j.cemconcomp.2020.103524.

Newell, D.L., Carey, J.W., 2013. Experimental evaluation of wellbore integrity along the cement-rock boundary. Environ. Sci. Technol. 47, 276–282. https://doi.org/10.1021/es3011404.

Okere, C.J., Sheng, J.J., Fan, L.K., et al., 2023. Experimental study on the degree and damage-control mechanisms of fuzzy-ball-induced damage in single and multi-layer commingled tight reservoirs. Pet. Sci. 20, 3598–3609. https://doi.org/10.1016/j.petsci.2023.05.017.

Peng, Z., Lv, F., Feng, Q., et al., 2022. Enhancing the CO_2-H_2S corrosion resistance of oil well cement with a modified epoxy resin. Constr. Build. Mater. 326, 126854. https://doi.org/10.1016/j.conbuildmat.2022.126854.

Ramadan, M. Al, Salehi, S., Ezeakacha, C., et al., 2019. Analytical and experimental investigation of the critical length in casing-liner overlap. Sustain. Times 11, 1–17. https://doi.org/10.3390/su11236861.

Schwartz, M.O., 2018. Le nouveau projet Wallula CO_2 pourrait relancer l'ancien projet de stockage de déchets nucléaires dans les basaltes de la Columbia River (ouest des Etats-Unis d'Amérique). Hydrogeol. J. 26, 3–6. https://doi.org/10.1007/s10040-017-1632-y.

Sigfússon, B., Arnarson, M.P., Snæbjörnsdóttir, S.Ó., et al., 2018. Reducing emissions of carbon dioxide and hydrogen sulphide at Hellisheidi power plant in 2014-2017 and the role of CarbFix in achieving the 2040 Iceland climate goals. Energy Proc. 146, 135–145. https://doi.org/10.1016/j.egypro.2018.07.018.

Su, X., Liu, S., Zhang, L., et al., 2023. Wellbore leakage risk management in CO_2 geological utilization and storage: a review. Energy Rev. 2, 100049. https://doi.org/10.1016/j.enrev.2023.100049.

Sun, X., Yao, Y., Ripepi, N., et al., 2018. A novel method for gas–water relative permeability measurement of coal using NMR relaxation. Transport Porous Media 124, 73–90. https://doi.org/10.1007/s11242-018-1053-y.

Taylor, H.F.W., 1965. The chemistry of cements. Mineral. Mag. J. Mineral Soc. 35, 434. https://doi.org/10.1180/minmag.1965.035.270.26.

Teng, Y., Liu, Y., Lu, G., et al., 2017. Experimental evaluation of injection pressure and flow rate effects on geological CO_2 sequestration using MRI. Energy Proc. 114, 4986–4993. https://doi.org/10.1016/j.egypro.2017.03.1642.

Um, W., Rod, K.A., Jung, H.B., 2012. Geochemical alteration of wellbore cement by CO_2 or CO_2+H_2S reaction during long-term carbon storage. Greenh. Gases Sci. Technol. 2, 352–368. https://doi.org/10.1002/ghg.

Wan, K., Xu, Q., Wang, Y., et al., 2014. 3D spatial distribution of the calcium carbonate caused by carbonation of cement paste. Cem. Concr. Compos. 45, 255–263. https://doi.org/10.1016/j.cemconcomp.2013.10.011.

Wang, N., Park, J., Evans, E.A., et al., 2014. Characterization of recycled rubber media for hydrogen sulphide (H_2S) control. Environ. Technol. 35, 2500–2505. https://doi.org/10.1080/09593330.2014.911359.

Wang, Y., Crandall, D., Bruner, K., et al., 2013. Core and pore scale characterization of Liujiagou Outcrop Sandstone, Ordos basin, China for CO_2 aquifer storage. Energy Proc. 37, 5055–5062. https://doi.org/10.1016/j.egypro.2013.06.419.

Wang, Y., Liu, S., Zhang, L., et al., 2021. Evidence of self-sealing in wellbore cement under geologic CO_2 storage conditions by micro-computed tomography (CT), scanning electron microscopy (SEM) and Raman observations. Appl. Geochem. 128, 104937. https://doi.org/10.1016/j.apgeochem.2021.104937.

Xu, B., Yuan, B., Wang, Y., 2018a. Anti-corrosion cement for sour gas (H_2S-CO_2) storage and production of HTHP deep wells. Appl. Geochem. 96, 155–163. https://doi.org/10.1016/j.apgeochem.2018.07.004.

Xu, B., Yuan, B., Wang, Y., et al., 2018b. H_2S-CO_2 mixture corrosion-resistant Fe_2O_3-amended wellbore cement for sour gas storage and production wells. Constr. Build. Mater. 188, 161–169. https://doi.org/10.1016/j.conbuildmat.2018.08.120.

Yan, Z., Okere, C.J., Zeng, X., et al., 2022. Preventing sour gas kicks during workover of natural gas wells from deep carbonate reservoirs with anti-hydrogen sulfide fuzzy-ball kill fluid. Energy Sci. Eng. 10, 2674–2688. https://doi.org/10.1002/ese3.1158.

Yin, Y., Zhang, L., Mei, K., et al., 2024. Experimental investigation on H_2S-induced oilwell cement degradation under high-temperature conditions for geothermal applications. Geothermics 121, 103023. https://doi.org/10.1016/j.geothermics.2024.103023.

Zhang, L., Dzombak, D.A., Nakles, D.V., et al., 2013a. Reactive transport modeling of interactions between acid gas (CO_2+H_2S) and pozzolan-amended wellbore cement under geologic carbon sequestration conditions. Energy Fuels 27, 6921–6937. https://doi.org/10.1021/ef401749x.

Zhang, L., Dzombak, D.A., Nakles, D.V., et al., 2013b. Characterization of pozzolan-amended wellbore cement exposed to CO_2 and H_2S gas mixtures under geologic carbon storage conditions. Int. J. Greenh. Gas Control 19, 358–368. https://doi.org/10.1016/j.ijggc.2013.09.004.

Zhang, L., Dzombak, D.A., Nakles, D.V., et al., 2014. Rate of H_2S and CO_2 attack on pozzolan-amended class H well cement under geologic sequestration conditions. Int. J. Greenh. Gas Control 27, 299–308. https://doi.org/10.1016/j.ijggc.2014.02.013.

Zhang, L., Nowak, W., Oladyshkin, S., et al., 2023. Opportunities and challenges in CO_2 geologic utilization and storage. Adv. Geo-Energy Res. 8, 141–145. https://doi.org/10.46690/ager.2023.06.01.